# Surface-Wave Metaprism for Smart Surface Communications

Talha Arshed, *Graduate Student Member, IEEE*, Stefano Maci, *Fellow, IEEE*, and Enrica Martini, *Senior Member, IEEE*

***Abstract*—We present a design technique and numerical validation for a surface-wave "metaprism" (MTP) acting as a frequency-dependent anomalous reflector for next-generation communications in a smart radio environment (SRE). This device holds promise for enabling physical layer frequency multiplexing and addressing waves in radio blockages. The proposed MTP is constituted by a passive and nonreconfigurable metasurface (MTS) comprising three sections. The first section (receiver) operates with low dispersion, receiving broadband signals coming from the base transceiver station (BTS) at a predefined angle and converting them into surface waves (SWs). The subsequent transition section gradually increases the dispersion of SW, guiding it toward the highly dispersive transmitter section, which finally converts the SW into space waves (SPWs) radiated toward frequency-dependent angular directions. The latter property motivates the name "MTP." MTP is implemented by an array of subwavelength metallic patches printed on a grounded dielectric slab, initially modeled using a homogenized penetrable impedance boundary condition (PIBC). The dispersion analysis of the MTS unit cell reveals the impact of patch geometry on dispersion characteristics, which is important for achieving broad scanning performance. Full-wave simulations validate the design, demonstrating high-power conversion efficiency and a reasonable frequency scan range. Moreover, the study compares the performance of SW-based MTP with that of a spatially dispersive reflecting intelligent surface (RIS), highlighting the advantages of MTP. In addition, this article investigates an "around the corner" design, where the SW reroutes the signal around a bent transition section, shading light on the relationship between SW dispersion and power loss due to edge diffraction.**

***Index Terms*—Antennas, Floquet waves (FWs), intelligent surfaces, leaky waves (LWs), metasurface (MTS), smart radio environment (SRE), surface waves (SWs).**

## I. Introduction

METASURFACES (MTSs) constitute a powerful and versatile platform to control electromagnetic fields [1], [2], [3], [4]. In particular, the ability to achieve anomalous reflection (AR), i.e., the reflection of an impinging space wave (SPW) in a nonspecular direction, through a periodically modulated MTS has been exploited to create reflecting intelligent surfaces (RISs), to be used as a potential enabling technology for smart radio environments (SREs) of the next generation (6G) of wireless communication system [5], [6]. The MTS–RIS is envisioned to be strategically placed on buildings, boards, and walls, to redirect impinging signals and create additional communication channels between the transmitter and the receiver. Several papers have explored this topic, focusing on the efficiency and angular range of AR [10], [11], [12], [13], [7], [8], [9]. The possibility of multiplexing different spatial frequencies and polarizations was also investigated [14], [15].

At the same time, it was observed that frequency dispersion can also play a role in the definition of the routing directions [16]. While some studies focused on the reduction of this effect [17], other authors have noted that this effect can be conveniently exploited to implement frequency-division multiplexing at the physical layer [18], [19]. However, this operation is difficult to implement using passive MTS–RIS, since for these devices the reflection angle variation is very weak for practical values of subcarrier separation and only depends on the incidence angle and MTS modulation period. As a result, the frequency behavior can only be engineered by introducing a complex circuitry [18], [19]. To overcome this issue, the proposed metaprism (MTP) works on the principle of double conversion, i.e., the impinging space wave (SPW) is first converted into a surface wave (SW) and then converted back from SW to a leaky wave (LW) in the desired direction. This approach not only offers a viable alternative solution to MTS–RIS but it also offers the possibility to tailor the frequency dispersion properties by controlling the value of the average surface impedance, thus, resulting in a better control over radiation direction and leakage.

The phenomenon of SW-to-SPW conversion (or vice versa) through a periodically modulated surface, which constitutes the fundamental operation in the proposed device, has been extensively studied in the literature [20], [21], [22], [23], [24], [25]. A pseudoanalytical model linking the propagation properties of radiated SPWs to the modulation parameters of a sinusoidally modulated scalar, nonpenetrable impedance boundary condition (PIBC) was first presented in Oliner's seminal work [20]. This model can be applied to describe modulated MTSs comprising dense arrays of subwavelength elements upon proper homogenization of BCs [26].

Received 11 December 2024; revised 18 April 2025; accepted 18 May 2025. Date of publication 2 June 2025; date of current version 8 September 2025. This work was supported by Italian Ministry of Universities and Research as part of the RESTART Project Framework. The work of Talha Arshed was supported by Italian Ministry of Universities and Research (Ministero dell'Università e della Ricerca) through the Programma Operativo Nazionale Ricerca e Innovazione 2014–2020 under Doctoral Grant. *(Corresponding author: Talha Arshed.)*

The authors are with the Department of Information Engineering and Mathematics, University of Siena, 53100 Siena, Italy (e-mail: talha.arshed@student.unisi.it; macis@dii.unisi.it; martini@dii.unisi.it).

Digital Object Identifier 10.1109/TAP.2025.3573607

The subsequent research has extended Oliner's method to treat penetrable IBCs [27], nonsinusoidal modulation functions [28], nonuniform modulation [29], [30], and tensorial IBC [27], thereby enabling significantly improved conversion efficiency, advanced beamforming, and polarization control [2], [27]. In antenna engineering, the conversion from guided SW to LW has recently led to a class of medium- to high-gain antennas known as modulated MTS antennas [31], [32], [33], [34], [35], [36]. The control of frequency dispersion in these antennas holds significance for two distinct applications: minimizing dispersion effects to achieve a stable beam across a desired frequency bandwidth [37], [38], [39], and, conversely, exploiting high dispersion to enable large-frequency scanning [40], [41], [42]. In [38], a ridge gap waveguide-based LW antenna (LWA) was presented, utilizing a series of microstrip branches as phase delay lines to compensate for dispersion effects. This design demonstrated a fractional bandwidth with a stable beam angle of 43%. Conversely, in another notable design [40], the LWA achieved a frequency scan of 152° within 2.2 GHz (equivalent to a scanning rate of 69°/GHz). The required high dispersion was achieved through a combination of glide symmetry and a single-layer Goubau line. On the other hand, the significant control over the frequency dispersion of SWs offered by MTSs has not yet been exploited as a design tool for creating frequency-dependent anomalous reflectors to be incorporated in multifrequency communication systems.

Indeed, wave rerouting through SW-based MTSs has not been extensively investigated in the literature; exceptions include [43], [44], [45], and [46]. In these works, the proposed devices are based on three sections: a receiver, a transition, and a transmitter sections. An early design [43] demonstrated a planar MTS device intercepting an SPW impinging at 30° at one segment and transmitting another SPW at –7.2° through the end segment, employing gradient surfaces for SPW-to-SW conversion. However, the overall rerouting efficiency achieved was limited to 10%. Kwon and Tretyakov [44] introduced an optimization approach to design impedance-modulated MTSs capable of receiving and retransmitting Gaussian beams at desired selected angles. Full-wave simulations of the MTS, modeled by a homogenized IBC, predicted an overall conversion efficiency close to 100%. However, the extremely rapid spatial variation in the synthesized impedance profile might hinder practical implementation. Notably, these designs focused solely on single-frequency operation rather than broadband scanning, which is instead the main focus of this study.

Unlike previous works in the literature, this article introduces a novel passive and static MTS device designed to receive a broadband wireless signal and transmit it toward frequency-dependent angular directions by employing a double conversion to/from SW. The objective is to enable physical layer orthogonal frequency-division multiplexing by properly assigning different subcarriers to various users [19]. Our MTS design relies on the design of continuous IBC profiles, that are finally implemented through printed patches on grounded dielectric. The process of attaining efficient SW–SPW (or SPW–SW) conversion via the appropriate impedance profile has been detailed in our earlier papers [30], [47]. Here, we expand upon this foundation, focusing on manipulating and controlling the dispersion characteristics of SWs on modulated IBC to create this innovative, simple, and low-cost "MTP." As in other studies related to SW-based rerouting, we adopt a three-part configuration comprising receiver, transition, and transmitter sections. To obtain the intended functionality, three distinct dispersion profiles are devised for each section: dispersion is very limited in the first section, to enable the simultaneous reception of multiple frequencies, while it is high in the transmitting section, to enhance frequency scanning. The transition section provides a smooth transition between the two regimes. After a first design was done at homogenized impedance level, a realistic implementation through patches printed on a grounded slab was carried out. An important result of this study is the correlation between SW dispersion and both the homogenized impedance values and the synthesized patch shapes. Comprehensive full-wave simulations were conducted on the final MTS device, confirming its effective performance. The broadband performance is compared with the one of MTS–RIS using direct AR.

In addition, we propose a simple yet effective solution to extend the applicability of the proposed device to a scenario, where the impinging SPW power is collected on one side of a building and must be rerouted to another shadowed side, to address radio blockages. This concept was studied in [45] using an MTS device with a conformal transition section designed to transfer an SW around a rounded corner. The reported full-wave simulation of the structure, carried out with a homogenized IBC, demonstrated an overall transfer efficiency close to 97.5%. The adopted design procedure relied on the numerical optimization of impedance boundary conditions and did not specifically addressed the relationship between SW dispersion and power transfer efficiency. In this article, the design of the bent MTP is carried out by propagating the SW along a sharp corner, where the power transfer efficiency is maximized by controlling the dispersion of the MTS covering the corner region.

This article is organized as follows. Section II formulates the problem and illustrates the working principle and design procedure for the proposed device. Section III presents numerical results. Finally, Section IV provides a summary of the conclusions and insights derived from this work.

## II. Working Principle and Design

### A. Problem Geometry

Fig. 1 shows the geometry and illustrates the fundamental working principle of the MTP proposed in this article. The planar MTP is placed on the *xy* plane of a Cartesian reference system. A linearly polarized incident wave impinges on the MTS at a predefined angle with an arbitrary amplitude distribution. This incident beam is envisioned as originating from a base transceiver station (BTS), and it has a frequency bandwidth capable of accommodating multiple subchannels, which will ultimately be rerouted to different users. Obstruction-induced masking effects (e.g., due to buildings) confine the beam propagation to a finite portion of the MTP, denoted as the receiving section. The key challenges within this segment lies

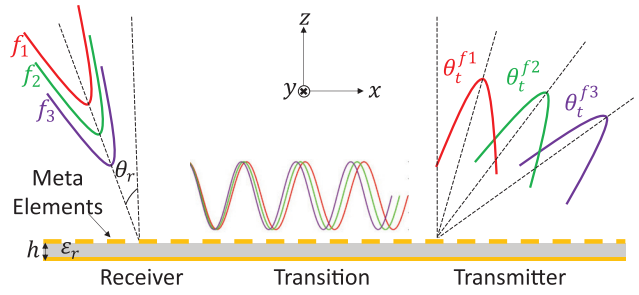


Fig. 1. Illustration of the working principle of the proposed MTP, which includes SPW-to-SW conversion, SW guidance, and frequency beam scanning.

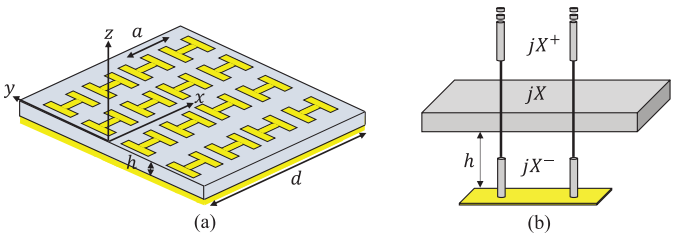


Fig. 2. (a) Geometry of patch-based MTS designed to support the propagation of a TM SW along the $x$-axis. (b) Equivalent transmission line model.

in effectively collecting the incoming power and transferring it to an SW, while minimizing losses due to scattering. In this respect, maintaining consistent conversion efficiency across the whole frequency band poses a challenge, due to the inherent dispersion of the modulated MTS, which should be minimized in this receiving section.

The transition section is intended to collect the SW from the receiving section and guide it along the $+x$-axis without radiation while progressively adjusting its wavenumber to match the one supported by the transmitting section.

Finally, the transmitting section is designed to emulate the performance of a high-frequency scanning rate LWA by using a highly dispersive MTS. In general, the frequency dispersion of printed MTSs can be easily controlled through the characteristics of the substrate. However, the challenge here is that the choice of the substrate will also affect the receiving section, for which frequency dispersion must be minimized. For this reason, the shape and size of the metaelements will be used to control the dispersion, as well as the leakage constant.

### B. Penetrable Impedance Boundary Condition

For implementation, a patch-type MTS is considered due to its compatibility with low-cost printed circuit board (PCB) technology. The MTS comprises infinitesimally thin subwavelength metallic patches printed on a planar grounded dielectric slab characterized by thickness $h$ and dielectric constant $\varepsilon_r$ [see Fig. 2(a)]. In the receiving (transmitting) section, the patches are periodically modulated along the $x$-axis to achieve SPW–SW (SW–SPW) conversion, while they remain invariant along the $y$-axis. Considering the case of linearly polarized waves, common in communication models, we assume an impinging electric field polarized along $x$. Due to their small electrical dimensions, the printed patches can be effectively substituted by their equivalent homogenized reactance during the design phase. Hence, the electromagnetic behavior of the printed metallic layer is accurately modeled using a PIBC. This model relates the average tangential electric field $E_x$ on the printed layer to the discontinuity of the average tangential magnetic field $H_y$ across it (or equivalently, the average current $J_x$ flowing on it)

$$E_x = jX\left(H_y|_{0^-} - H_y|_{0^+}\right) = jXJ_x. \tag{1}$$

Here, $X$ represents the homogenized reactance of the metallic cladding, which is capacitive for a patch-type MTS. A uniform array of patches, represented by a constant reactance $X(x) = X^{(0)}$, supports a transverse magnetic (TM) SW characterized by a longitudinal propagation constant $k_x = \beta_{SW} > k_0$, where $k_0$ is the free SPW number, and an attenuation constant $\alpha_z$ orthogonal to the MTS, with an associated current of the form $J_x(x) = J_x^{(0)} e^{-j\beta_{SW}x}$. The dependency of the propagation constant on the angular frequency $\omega$ is given by the transverse resonance equation of the structure, which reads

$$\frac{1}{X^+(\beta_{SW})} + \frac{1}{X^-(\beta_{SW})} + \frac{1}{X^{(0)}} = 0 \tag{2}$$

where $X^+(\beta_{SW})$ and $X^-(\beta_{SW})$ are the TM reactances of a $z$-directed transmission line toward free space and toward the ground, respectively [see Fig. 2(b)], i.e.,

$$X^+(\beta_{SW}) = -\zeta \frac{\sqrt{\beta_{SW}^2 - k_0^2}}{k_0} \tag{3}$$

$$X^-(\beta_{SW}) = \zeta \frac{\sqrt{\epsilon_r k_0^2 - \beta_{SW}^2}}{k_0 \epsilon_r} \tan\left(h\sqrt{\epsilon_r k_0^2 - \beta_{SW}^2}\right) \tag{4}$$

where $\zeta_0$ is the free space impedance that is equal to 377 Ω.

### C. Synthesis of PIBC for SPW–SW Conversion

This section provides a summary of the SW-to-SPW conversion model employing modulated impedance based on our adaptation of Oliner's method [20] to nonuniform modulation and PIBC [27]. Recognizing the reciprocal nature of SPW-to-SW and SW-to-SPW conversions, the description of the design process will focus on SW-to-LW conversion, as this can then be seamlessly adapted to the reciprocal receiving mode.

Typically, a source generates an SW traveling on a constant reactance $X^{(0)}$ with a related propagation constant $\beta_x^{(0)}$, and this SW undergoes a transformation upon entering a region with modulated reactance. This transformation results in a wave represented as an infinite series of Floquet harmonics [Floquet waves (FWs)]. The complex propagation constant of the $n$th FW is defined as $k_x^{(n)} = \beta_x^{(n)} - j\alpha_x$, with $\beta_x^{(n)} = \beta_x^{(0)} + 2\pi n/d$. For a proper design, only the -1-indexed FW should fall within the visible spectral region, thus, giving rise to the leakage constant $\alpha_x$, common to all FWs, which is physically necessary to balance the power transfer from SW to LW.

Achieving a precise distribution of $\alpha_x(x)$ and $\beta_x^{(-1)}(x)$ across the aperture is essential for realizing an efficient SW-to-SPW conversion. To this end, the design process follows this sequence [30]: first, the magnitude $A(x)$ and phase $\phi(x)$ of the aperture field are derived from the intended radiation pattern (or, reciprocally, from the incident field). Next, $\alpha(x)$

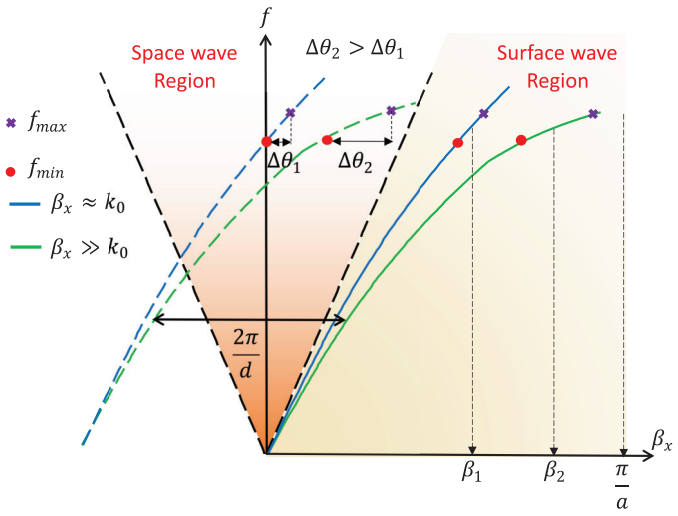


Fig. 3. Illustration of the dispersion diagram of the TM modes supported by modulated MTSs characterized by a unit cell size $a$ and a modulation period $d$. Continuous and dashed lines represent 0- and -1-indexed FWs, respectively.

and $\beta_x^{(-1)}(x)$ are derived from $A(x)$ and $\phi(x)$. Subsequently, the local modulation index $m(x)$ and period $d(x)$ are obtained from $\alpha(x)$ and $\beta_x^{(-1)}(x)$ by solving the corresponding local canonical problem with sinusoidal modulation. Finally, the overall reactance profile $X(x)$ is calculated through [30]

$$X(x) = X^{(0)}\left[1 + m(x)\cos\left(\int_0^x \frac{2\pi}{d(x')}dx'\right)\right]. \tag{5}$$

In (5), $d(x) = 2\pi/\beta_x^{(0)}(x)$, where $\beta_x^{(0)} = \beta_{SW} + \Delta\beta$ has a small deviation $\Delta\beta$ with respect to the value $\beta_{SW}$ corresponding to the average reactance $X^{(0)}$. This deviation, which depends on $m$, $d$, and $X^{(0)}$, although small with respect to $\beta_{SW}$, becomes important for large apertures, as the phase error accumulates along the SW path.

### D. Frequency Dispersion

The dispersion diagram serves as a valuable tool for analyzing the frequency dispersion of a MTS. For modulated MTSs, we consider the dispersion curve associated with the average reactance $X^{(0)}$. These curves are calculated by solving the dispersion equation (2).

As an illustrative example, the blue and green continuous lines in Fig. 3 depict the dispersion curves of two SWs supported by MTSs with different values of penetrable reactance $X^{(0)}$ and the same unit cell size $a$. In particular, the green curve is associated with a lower absolute value of $X^{(0)}$ (i.e., a larger capacitance), and therefore, it exhibits a lower slope, which corresponds to a lower group velocity $v_g$. The values of $\beta_x$ at two frequencies ($f_{min}$) and ($f_{max}$) delimiting the operative bandwidth can be linked to each other by the following equation, using a first-order Taylor-type linear approximation:

$$\beta_x(f_{max}) \simeq \beta_x(f_{min}) + \frac{2\pi\Delta f}{v_g} \tag{6}$$

where $\Delta f = f_{max} - f_{min}$ and $v_g$ is the group velocity at the minimum frequency. Equation (6) clearly indicates that the lower the group velocity, the greater the frequency dispersion of the structure.

When a periodic modulation of period $d$ is introduced, the dispersion curve of the dominant mode is almost unperturbed, while other replica shifted by integer multiples of $(2\pi)/d$ appear. In particular, the curves relevant to the -1-indexed mode are shown in Fig. 3 by the dashed lines. Part of these curves falls within the visible region (VR), delimited by the two black dashed lines. For a given frequency, each point in the VR corresponds to a different LW pointing angle $\theta$, referred to hereafter as the *scanning angle*, according to the relationship $\beta_x^{(-1)} = k_0 \sin(\theta)$. The relationship between the maximum angle $\theta_{max} = \theta(f_{max})$ and the minimum angle $\theta_{min} = \theta(f_{min})$ of the scanning range is therefore

$$f_{max}\sin\theta_{max} - f_{min}\sin\theta_{min} \simeq \frac{c_0}{v_g}\Delta f \tag{7}$$

where $c_0$ is the speed of light in free space. Equation (7) shows that a lower group velocity (i.e., a greater dispersion) leads to a larger angular scanning. The implication is that, for an effective MTP implementation, a low group velocity is required in the receiving section, while a high group velocity is needed in the transmitting section.

## III. Numerical Results

In this section, we illustrate the design of an MTP operating at a central frequency of 26 GHz (5G mmWave band) with a bandwidth of 500 MHz. For MTS implementation, we consider a grounded substrate with relative dielectric constant $\epsilon_r = 6$ and height $h = 0.508$ mm. A modulated MTS implemented with printed elements exhibits a double periodicity scale [27]. The subwavelength microperiod ($a$) pertains to the constitutive unit cell, and is used to synthesize the desired homogenized penetrable impedance. On the other hand, the macroperiod ($d$) is used to implement the local modulation, under the assumption of homogenized impedance. Following the conclusion of Section II-D, different average reactance values are chosen for the receiving and the transmitting section, with the first one being much bigger in magnitude. In the transmitting section, the geometry of the patch elements plays a fundamental role in the determination of the frequency dispersion properties, as illustrated in the next section.

### A. Dispersion Analysis of the MTS Unit Cell

This section discusses the choice of the patch geometry for obtaining enhanced frequency dispersion in the transmitting section. As illustrated in Fig. 3, the dispersion curve becomes highly dispersive when $\beta_x$ approaches the limit of the first Brillouin zone $\beta_x \approx \pi/a$. However, in practice, that region is also characterized by large sensitivity to fabrication inaccuracies and possibly enhanced losses. As a compromise, aiming at a unit cell size in the range $[\lambda/10, \lambda/5]$, a representative wavenumber for the transmitting section can be $\beta_x = 1.85k_0$, which, according to (2), corresponds to $X^{(0)} = -50\ \Omega$.

A key design requirement for achieving large-frequency scanning in MTS systems is the realization of a unit cell with a low-group velocity, as shown in (7). To illustrate this, three-unit cell geometries—H-shaped, slotted rectangle, and annular

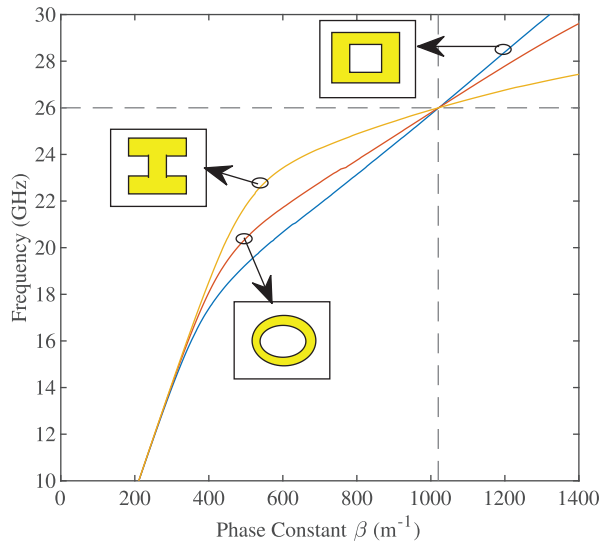


Fig. 4. Dispersion diagram for different unit cells: H-shaped, slotted rectangle, and annular ring.

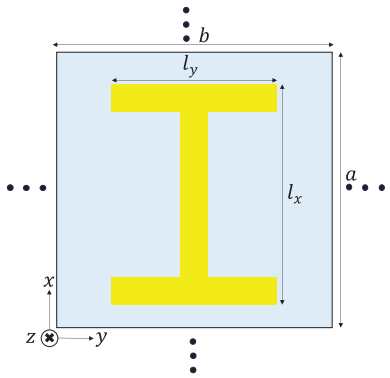


Fig. 5. Geometry of the H-shaped patch unit cell designed to support TM SW propagating along the $x$-axis.

ring—were engineered to achieve a wavenumber of $1.85k_0$ at 26 GHz. These geometries were rigorously analyzed in a periodic environment using the spectral method of moments (MoM) described in [48], and the corresponding dispersion diagrams are presented in Fig. 4. The results indicate that the H-shaped unit cell exhibits the lowest group velocity (i.e., the flattest dispersion curve) at 26 GHz, whereas the slotted rectangle yields the highest group velocity. In Section III-B, it is demonstrated that MTPs designed with an identical impedance profile but implemented with different unit cell geometries exhibit markedly different frequency scanning characteristics.

Owing to its design flexibility and high dispersion capability, the H-shaped patch—as illustrated in Fig. 5—was selected for further investigation. This unit cell was analyzed using the aforementioned periodic MoM code. After identifying different combinations of geometrical parameters providing the desired equivalent reactance at the working frequency, frequency dispersion is investigated.

Table I summarizes the results of our numerical investigations. The dispersion characteristics are quantified by $(\Delta f/\Delta\beta_x)\cdot(2\pi/c_0) \simeq v_g/c_0$, calculated using our MoM routine.

TABLE I

GROUP VELOCITY AS A FUNCTION OF GEOMETRICAL PARAMETERS FOR THE H-SHAPED PATCH

| Input Parameters $f_c = 26$ GHz, $\epsilon_r = 6$, $h = 0.508$ mm, $X^{(0)} = -50\ \Omega$ | | | | |
|---|---|---|---|---|
| *Set I* | | | | |
| $a(mm)$ | $b(mm)$ | $l_x(mm)$ | $l_y(mm)$ | $v_g/c_0$ |
| 1.2 | 1.2 | 1.15 | 1.15 | 0.229 |
| 1.7 | 1.7 | 1.3 | 1.3 | 0.115 |
| *Set II* | | | | |
| 1.7 | 1.7 | 1.17 | 1.6 | 0.092 |
| 1.7 | 1.7 | 1.6 | 0.88 | 0.204 |
| *Set III* | | | | |
| 1.4 | 1.7 | 1.21 | 1.3 | 0.157 |
| 1.7 | 1.4 | 1.34 | 1.3 | 0.134 |

TABLE II

CALCULATED CONVERSION EFFICIENCIES FOR MTP

| Freq. (GHz) | **25.75** | **25.875** | **26** | **26.125** | **26.25** |
|---|---|---|---|---|---|
| $P_{SW}^{(rx)}/P_{in}$ | 63.1% | 86.2% | 93.6% | 84.4% | 72% |
| $P_{SW}^{(tx)}/P_{in}$ | 60.8% | 83% | 90% | 81.3% | 69% |
| $P_{SPW}^{(tx)}/P_{in}$ | 57% | 76% | 84.6% | 76.2% | 67.5% |

Data from set I show that, for a square unit cell ($a = b$), increasing the size leads to a larger dispersion, as increasing $a$ brings the operation point on the dispersion curve closer to the edge of the first Brillouin zone. Data from Set II show that a distinctive feature of the H-shaped patch is that, for a given unit cell size, increasing the parameter $l_y$ instead of $l_x$ leads to a greater dispersion. Finally, data from set III explore the impact on the dispersion of adopting a rectangular unit cell instead of a square one. As expected, for a fixed length of $l_y$, a larger side ($a$) along the propagation direction, accompanied by a larger value of $l_x$, increases the dispersion, although the difference is less remarkable than for the previous two sets.

### B. Full-Wave Analysis of Patch-Type MTP Implementation

This section presents the design and full-wave simulation of a planar MTP. The planar structure extends along the $xy$ plane and is modulated along the $x$-axis. The incoming signal is here modeled as a Gaussian-beam waveform impinging from the direction is set to $\theta_r = -10°$, leading to the following amplitude distribution for the incident field on the MTP plane

$$A(x) = Ae^{-(x-L/2)^2/2\sigma^2} \tag{8}$$

with a beam waist of $\sigma\sqrt{2} = \sqrt{2} \times 16\lambda/3$. This model describes a scenario where an external obstacle produces a partial masking of the field radiated by the BTS, so that only a portion of the MTS is exposed to the impinging wave.

The length of the receiver section is set to $L_r = 32\lambda$. For this section, the tangential wavenumber $\beta_r^{(0)} = 1.08k_0$ is chosen to guarantee low dispersion. Similarly, for the transmitter section, the length is set to $L_t = 32\lambda$, while the tangential wavenumber is chosen to be $\beta_t^{(0)} = 1.98k_0$ to enhance frequency dispersion. The transmission angle is set to 45° for the central frequency. Finally, the transition section is required to progressively adapt the SW wavenumber in the receiving section to the one of the transmitting section. Our design goal was to optimize

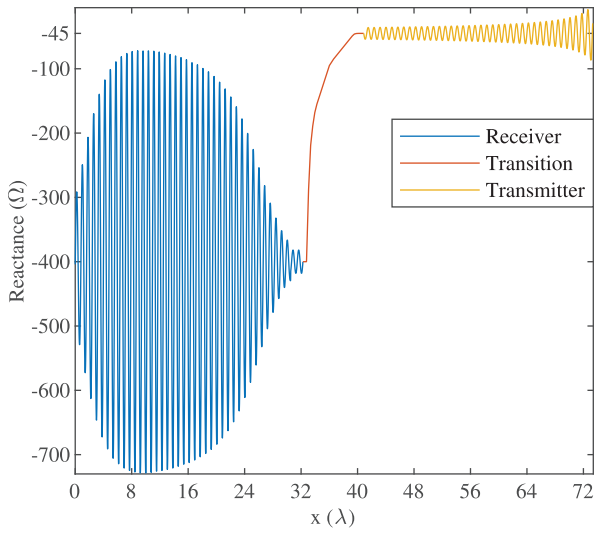


Fig. 6. Synthesized reactance profile for MTP.

the matching efficiency while keeping the transition section as compact as possible, to maximize the overall aperture efficiency. Through our analysis, we determined that increasing the wavenumber with a constant gradient of $0.21\,k_0$ per $\lambda$ over a $9\lambda$ long transition section provides an optimal balance between performance and size. Our numerical results indicate that this design choice results in a power loss of approximately 3.6% at the central frequency; a shorter transition section would have led to higher losses.

The penetrable reactance profile ($X(x)$) synthesized by applying (5) with the above input parameters is shown in Fig. 6. The receiver, transition, and transmitter reactances are represented in blue, orange, and yellow lines, respectively. The average reactance for the receiver and transmitter sections are $X_r^{(0)} = -400\ \Omega$ and $X_t^{(0)} = -45\ \Omega$, respectively, while the transition profile is nonmodulated and is designed to gently transition from the first average reactance to the second one.

The receiving section exhibits stronger reactance fluctuations than the transmitting one due to its larger average reactance (-450 versus $-45\ \Omega$), which amplifies absolute variations under identical modulation indexes. Furthermore, the nonlinear interdependence between modulation index ($m$), average reactance ($X_0$), and leakage constant ($\alpha$) (as calculated by solving [30, eq. (14)]) dictates that higher $|X_0|$ values in the receiver require increased $m$ to maintain target $\alpha$ levels, further accentuating fluctuations.

As a next step, the synthesized reactance profile is implemented by H-shaped patches. Based on the analysis carried out in Section III-A, the implementation of the reactance profile for the receiver section requires the use of low values of $l_y$ and high values of $l_x$. Conversely, the transmitter section requires higher values of $l_y$. Moreover, rectangular unit cells are used for the receiver section, with a smaller side along the propagation direction, to achieve lower dispersion and, thus, increased angular stability. More specifically, based on the dispersion analysis, the dimensions of the unit cells for the receiver and transmitter sections are set to $1.2 \times 1.7$ mm$^2$ and $1.7 \times 1.7$ mm$^2$, respectively.

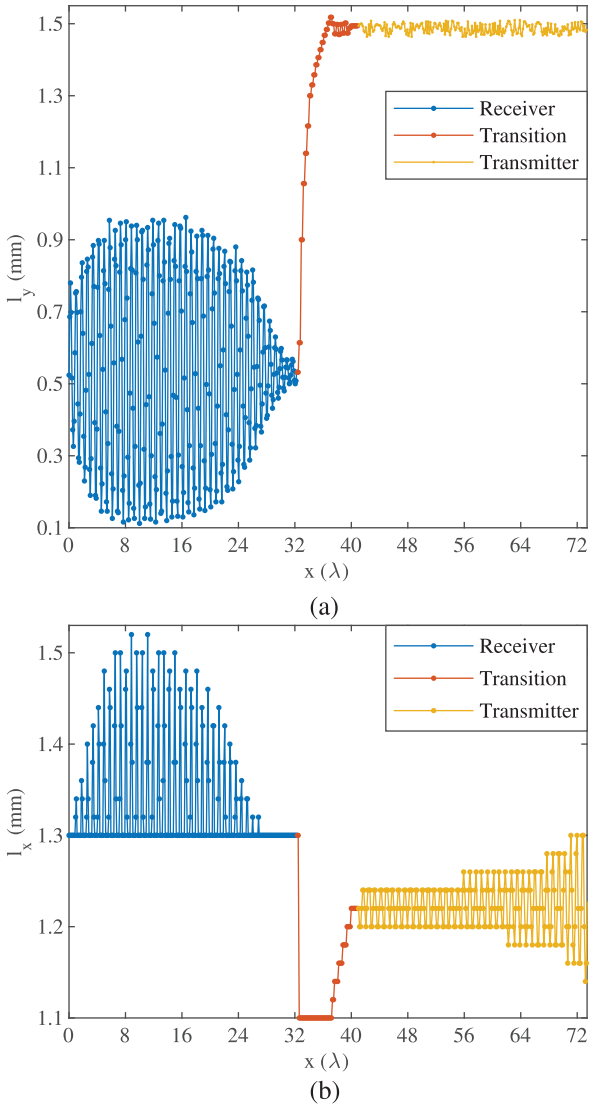


Fig. 7. Layout of unit's cell parameters (a) $l_y$ and (b) $l_x$ as a function of $x$.

To implement the reactance profile, we discretize it with a sampling step equal to the unit cell size and assign a corresponding unit cell geometry to each sample. This is achieved by constructing a database of H-shaped unit cells, where the key parameters $l_x$ and $l_y$ (as shown in Fig. 5) are varied, and their corresponding reactance values are computed using MoM code. Once the database is generated, each reactance sample is matched to the unit cell geometry that best approximates it. The selected unit cells are then sequentially arranged along the $x$-axis, as illustrated in Fig. 7. The structure comprises 310, 58, and 220 unit cells for the receiver, transition, and transmitter sections, respectively.

Full-wave simulations of the resulting structure are finally performed using the Ansys HFSS software package. There, perfect magnetic boundaries are placed orthogonal to the $y$-direction exploiting the periodicity along the $y$-axis, and the TM nature of the wave.

Fig. 8 depicts the magnitude of the incident tangential magnetic field ($H_y$) obtained at $f_c$ from the simulation. Fig. 8(a) shows the incident field at the central frequency

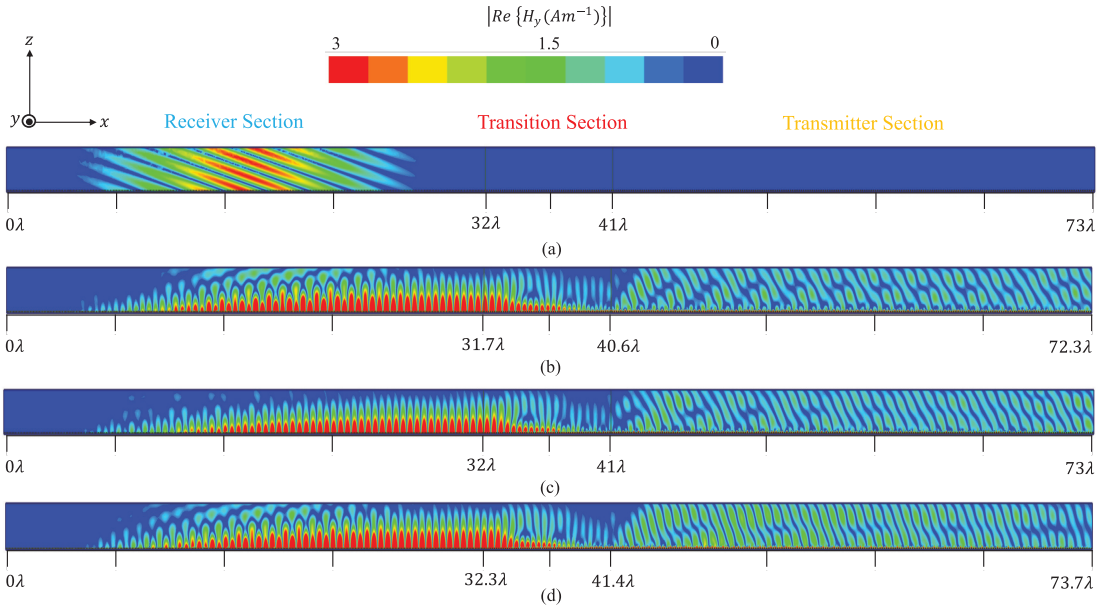


Fig. 8. Simulated $H$-field for the MTP. (a) Incident field. (b) Scattered field at 25.75 GHz. (c) Scattered field at 26 GHz. (d) Scattered field at 26.25 GHz.

$f_c$, corresponding to the scattered field reported in Fig. 8(c). Fig. 8(b) and (d) shows the scattered field at the minimum and maximum frequencies of the considered band, respectively.

In the scattered field photographs, we can see the SW propagating along the $x$-axis with a gentle progressive increase in magnitude over the receiver section, due to the gradual conversion of power density from the impinging Gaussian beam to the local SW. Furthermore, it is observed that as the SW crosses the transition section, it becomes increasingly confined to the surface, indicating an increase in its SW wavenumber. Finally, a radiated SPW emerging from the transmitter section in a frequency-dependent direction is observed.

Table II shows the conversion efficiencies at different frequencies across the considered bandwidth. In this table, the symbols have the following meaning.

1) $P_{in}$ is the power of the impinging SPW.
2) $P_{SW}^{(rx)}$ is the power of SW exiting the receiver section.
3) $P_{SW}^{(tx)}$ is the power of SW exiting the transition section.
4) $P_{SPW}^{(tx)}$ is the power of SPW radiated by the transmission section.

At the central frequency $f_c$, the incident Gaussian beam carries a power $P_{in} = 1$ W, and the SW power calculated in the $x = 32\lambda$ plane is $P_{SW}^{(rx)} = 0.936$ W, resulting in an SPW-to-SW conversion efficiency of 93.6%. The radiated power calculated in the $z = 1.5\lambda$ plane is $P_{SPW}^{(tx)} = 0.846$ W, resulting in an overall SPW–SW–SPW conversion efficiency of 84.6%. The overall efficiency drops by 27.6% at the lower edge of the bandwidth.

Fig. 9(a) illustrates the simulated directivity patterns at five frequencies across the considered bandwidth. For each frequency, along with the intended transmitted beam, a specularly reflected beam is also observed, due to nonperfect conversion of the impinging wave. At $f_c$, the ratio of the transmitted lobe to the reflected lobe is -17.8 dB. Importantly, the pointing angle of the main beam scans the range of $\Delta\theta_r = 14.6°$ (from 38.3° to 52.9°) across the bandwidth. This corresponds to a scanning rate per percentage of relative bandwidth of $\Delta\theta_r/\% = 7.592°$.

Notably, an MTP based on slotted rectangle unit cells, implementing the same impedance profile, exhibited a significantly reduced $\Delta\theta_r$ of only 4.5°, as shown in Fig. 9(b). These results not only confirm the scanning capability of the proposed MTP, thereby validating the design but also highlight the critical role of unit cell engineering in achieving the desired broadband performance.

### C. Comparison With a Nonspecular Reflective Surface

Nonspecular reflective surfaces based on MTSs currently constitute the prevalent technology for implementing RIS. Unlike the SW-based structure proposed here, in a MTS-based nonspecular reflector the entire structure can collect the incoming SPW power and redirect it nonspecularly thanks to a linear variation of the reflection coefficient phase. This implies a higher aperture efficiency at a single frequency. However, this solution presents a limited capability for physical layer frequency multiplexing [16], [49], [50], as will be shown in this section. The standard approach to achieve AR employs the generalized Snell's law as detailed in [7]. For given intended incidence ($\theta_i$) and reflected ($\theta_r$) angles, this leads to the following design equation (see [8, eq. (47)]) for the reactance $X_I(x)$ of the impenetrable impedance boundary condition (IIBC):

$$X_I(x) = Z_0^{TM} \cot\left[\frac{k_0 x}{2}(\sin\theta_i - \sin\theta_r)\right] \tag{9}$$

where $Z_0^{TM} = \zeta(k_{z0}/k_0)$, with $k_{z0} = k_0 \cos\theta_i$, represents the TM free space impedance for the incident wave. In order to incorporate spatial dispersion effects, and hence obtain better accuracy [11], the reactance of the IIBC in (9) is transformed

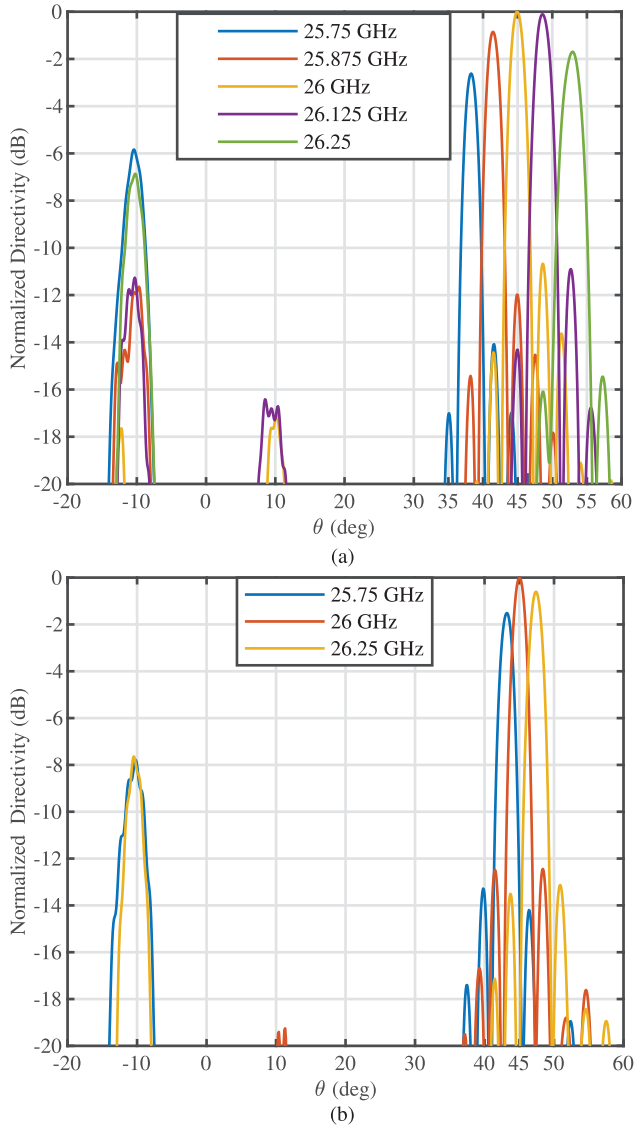


Fig. 9. Normalized directivity pattern for the MTP across the frequency band. (a) Implementation with an H-shaped unit cell. (b) Implementation with a slotted square unit cell.

(using [12, eqs. (4)–(9)]) into a penetrable reactance $X_P$ on top of a grounded slab by

$$X_P = \left[ \frac{1}{X_I} - \frac{\epsilon_r \cot\left(k_0 h \sqrt{\epsilon_r - \sin^2\theta_i}\right)}{\zeta \sqrt{\epsilon_r - \sin^2\theta_i}} \right]^{-1}. \quad (10)$$

In this case, the reflection angle is completely determined by the incidence angle, the frequency, and the modulation period, with no additional degrees of freedom, as opposed to the MTP, where one can play with MTS dispersion [see (7)]. Indeed, the angular range (see [12, eq. (5)]) of frequency scanning in the band $[f_1, f_2]$ is given by

$$\Delta\theta_r = \sin^{-1}\left(\sin\theta_i - \frac{c_0}{f_2 d}\right) - \sin^{-1}\left(\sin\theta_i - \frac{c_0}{f_1 d}\right). \quad (11)$$

In order to numerically compare this solution with the proposed MTP, (9) and (10) are applied to obtain the reactance profile corresponding to $\theta_i = -10°$ and $\theta_r = 45°$ keeping

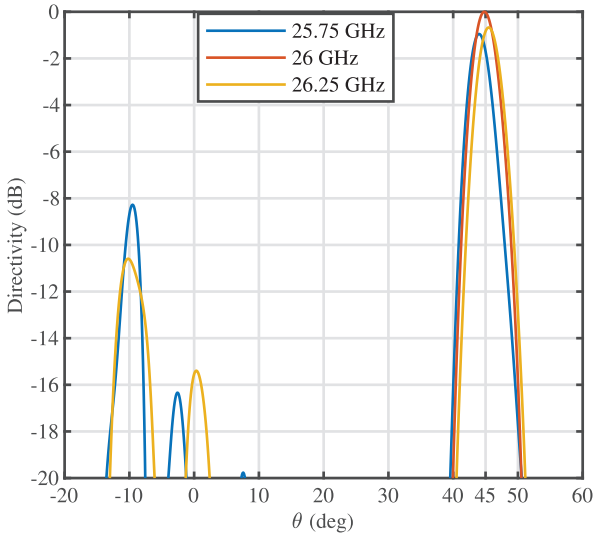


Fig. 10. Normalized directivity pattern for the nonspecular reflective surface-based MTS across the frequency band.

the other input parameters ($f_c$, $h$, and $\epsilon_r$) and excitation consistent with those of the SW-based MTP. Subsequently, an H-shaped patch-type MTS is designed based on this profile and simulated in HFSS. The structure length is kept the same as the length of the transmitter section of the SW-based MTS, i.e., $32\lambda$. The simulated directivity patterns of the field scattered by the nonspecular reflective surface-based MTS at different frequencies are shown in Fig. 10. As predicted by (11), the extracted value of $\Delta\theta_r/\%$ is 0.754°, which is significantly lower than the 7.792° achieved by the SW-based MTP. For context, state-of-the-art broadband MTS reflectors [16], [49], [50] report $\Delta\theta_r/\%$ values below 0.53°—consistent with the theoretical limit in (11). In contrast, the proposed SW-based MTP demonstrates a 10.4-fold improvement in the angular scanning efficiency over conventional designs.

### D. Full-Wave Analysis of Bent SW-Based MTP

In this section, we present the design and analysis of an MTP bent at a 90° angle, which is of interest for scenarios where the system architecture requires noncoplanar receiving and transmitting surfaces, e.g., corresponding to different walls of the same building [45], [51]. The proposed solution includes the corner, covered by a uniform reactance, in the transition section of the MTP, leveraging the capability of SWs to be guided by a nonplanar surface. The key challenge is to ensure that the SW gliding through the corner experiences minimal power loss due to diffraction. To this end, leveraging the equivalent impedance model of the MTS, our design strategy builds on the work in [52], which studied SW diffraction by an impedance wedge, to investigate the relationship between SW wavenumber and power loss due to diffraction at the bent.

The HFSS simulation setup for the analysis of the corner region is as follows: the structure contains two flat MTSs, the first one lies in the $xy$ plane, with a length of $5\lambda$ along the $x$-axis, while the second one lies in the $zy$ plane, with a length of $5\lambda$. The two MTSs are connected by a sharp 90° bend. An SW propagates along the $+x$-axis and enters the first MTS

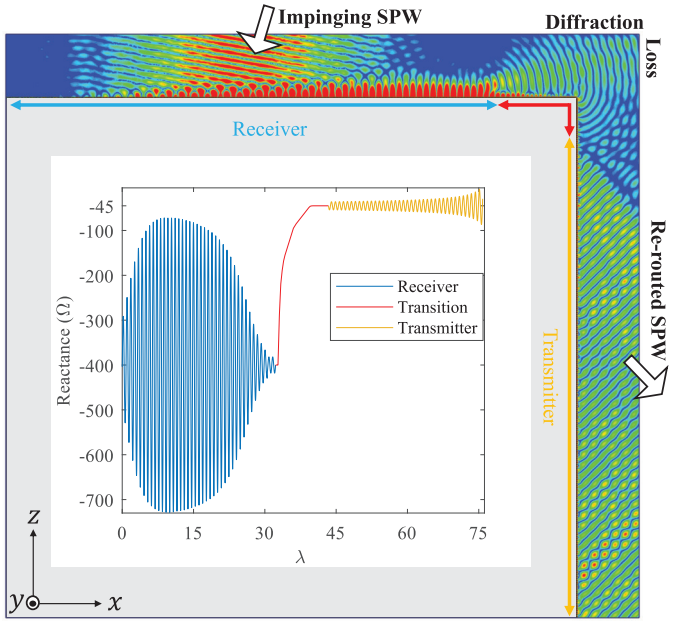


Fig. 11. Simulated $H$-field for the MTP bent at a 90° angle at the central frequency. Inset: impedance profile of the bent-MTP.

from $Port_1$. In the ideal case, as the SW crosses the bend it continues its propagation along the $-z$-axis until reaching $Port_2$.

Full-wave simulations are conducted for two different reactance values. In the first case, we have $X^{(0)} = -300\ \Omega$, meaning that the MTS in the $xy$ plane supports an SW with transverse propagation constant $\beta_x = 1.07k_0$ and longitudinal attenuation constant $\alpha_z = -0.38k_0$. In the second case, $X^{(0)} = -25\ \Omega$, corresponding to $\beta_x = 2.15k_0$ and $\alpha_z = -1.9k_0$. Full-wave simulations of the two structures reveal larger diffraction losses for the first case, with transmission coefficient between the two ports: $S_{21} = -8$ dB versus $S_{21} = -0.5$ dB for the second case. This difference is attributed to the larger attenuation along the direction normal to the surface in the second case. Indeed, this implies a tighter confinement of SW fields to the surface, resulting in reduced power leakage due to diffraction as the wave travels across the corner. These results suggest that a simple yet effective method of guiding SWs around the corner consists of using values of impedance corresponding to large SW wavenumber. In this connection, we can reuse results from Section III-B, where we demonstrated the ability to precisely achieve any desired value of the SW wavenumber on the patch-type MTS, guided by our MoM routine.

The approach described above is applied to design the target MTP with beyond-the-corner wave-routing capability. The receiver and transmitter sections are now on two different faces of a 90° wedge, with the transition section across the edge. Input parameters for the receiver and transmitter sections are kept identical from the previous example. For this design, the transition section is slightly elongated, with its bent region designed to support SWs with a high wavenumber ($\beta_t^{(0)} = 1.98k_0$). The simulated $H$-field of the structure at the central frequency is shown in Fig. 11. We can see that the majority of the power incident on the $xy$ aperture is collected, guided through the corner, and finally radiated from the $xz$ aperture. Based on the full-wave analysis, the calculated overall space-routing efficiency of the MTS implemented with H-shaped patches was 80% at the central frequency. The directivity pattern analysis (not included here for brevity) reveals that the radiation lobe corresponding to the rerouted wave is 13.4 dB higher than the diffraction lobe. In addition, the bent MTP design retains its frequency-scanning functionality over the operational bandwidth. The scanning angle for the bent-MTP is calculated to be 14.9° (analogous to that of the flat configuration), ranging from 128.1° to 143°. Moreover, the overall conversion efficiencies at the two edge frequency points are 52% and 50%, respectively.

## IV. Conclusion

The designs of a passive nonreconfigurable MTS device able to reroute different subcarriers of an incident beam toward different users (MTP) have been proposed. The device exploits a double conversion process, from SPW to SW and back to SPW, and leverages the dispersion properties intrinsic to SW propagation. Moreover, it has been demonstrated that appropriate dispersion control can minimize diffraction losses for SW propagating along a nonplanar path, thereby facilitating the rerouting of SPW around the wedges of buildings.

The proposed concept was implemented using readily accessible microstrip technology, featuring metallic patches on the grounded dielectric. For the initial design, the structure has been modeled using PIBC, and the relevant modulation parameters are determined based on the requirements of SW-to-SPW conversion at the center frequency and dispersion properties over a given bandwidth. Then, the dimensions of patch elements are determined through a detailed numerical dispersion analysis of the patch unit cell. Importantly, these design steps can be adapted for other fabrication technologies resorting to an IIBC model.

The full-wave analysis has been conducted on the patch-type MTSs using an HFSS simulator for validation. In the case of the MTP, the overall transmission efficiency was found to be 84.6% at the central frequency of 26 GHz, decreasing to 57% at the bandwidth edge (25.75 GHz), with an angular scanning range of 14.6° over a 1.92% fractional bandwidth. Although the incoming signal was modeled as a Gaussian-beam waveform, the design approach can be generalized to accommodate any arbitrary waveform. Future designs could enhance bandwidth performance via multilayer architectures, where a secondary MTS layer compensates frequency-dependent angle variations to sustain efficiency across wideband.

For the sake of comparison, simulations were also performed for an MTS-based anomalous reflector. In that case, the calculated angular scanning range was 1.5° for similar parameters. Furthermore, the design of an MTP featuring a 90° bent was also presented, with the ability to receive an incident SPW at one plane and subsequently radiate the captured power from the perpendicular plane. In this case, full-wave simulations showed an overall efficiency of 80%.

Based on the findings of this study, the proposed MTP concept shows potential for SRE applications by enabling

physical-layer frequency multiplexing. In addition, frequency-dependent wireless signal rerouting can be applied in the wireless localization domain. Additional functionalities can be obtained by incorporating active reconfiguration into the SW-based MTS.

## REFERENCES


[1] C. L. Holloway, E. F. Kuester, J. A. Gordon, J. O'Hara, J. Booth, and D. R. Smith, "An overview of the theory and applications of metasurfaces: The two-dimensional equivalents of metamaterials," *IEEE Antennas Propag. Mag.*, vol. 54, no. 2, pp. 10–35, Apr. 2012.

[2] E. Martini and S. Maci, "Modulated metasurfaces for microwave field manipulation: Models, applications, and design procedures," *IEEE J. Microw.*, vol. 2, no. 1, pp. 44–56, Jan. 2022.

[3] M. Khalily, O. Yurduseven, T. J. Cui, Y. Hao, and G. V. Eleftheriades, "Engineered electromagnetic metasurfaces in wireless communications: Applications, research frontiers and future directions," *IEEE Commun. Mag.*, vol. 60, no. 10, pp. 88–94, Oct. 2022.

[4] S. Maci, "Electromagnetic metamaterials and metasurfaces: A historical journey," *IEEE Antennas Propag. Mag.*, vol. 66, no. 3, pp. 84–101, Jun. 2024.

[5] Q. Wu and R. Zhang, "Towards smart and reconfigurable environment: Intelligent reflecting surface aided wireless network," *IEEE Commun. Mag.*, vol. 58, no. 1, pp. 106–112, Jan. 2020.

[6] N. Shlezinger, G. C. Alexandropoulos, M. F. Imani, Y. C. Eldar, and D. R. Smith, "Dynamic metasurface antennas for 6G extreme massive MIMO communications," *IEEE Wireless Commun.*, vol. 28, no. 2, pp. 106–113, Apr. 2021.

[7] N. Yu et al., "Light propagation with phase discontinuities: Generalized laws of reflection and refraction," *Science*, vol. 334, no. 6054, pp. 333–337, Oct. 2011. [Online]. Available: https://www.science.org/doi/abs/10.1126/science.1210713

[8] V. S. Asadchy, M. Albooyeh, S. N. Tcvetkova, A. Díaz-Rubio, Y. Ra'di, and S. A. Tretyakov, "Perfect control of reflection and refraction using spatially dispersive metasurfaces," *Phys. Rev. B, Condens. Matter*, vol. 94, no. 7, Aug. 2016, Art. no. 075142.

[9] A. Epstein and G. V. Eleftheriades, "Synthesis of passive lossless metasurfaces using auxiliary fields for reflectionless beam splitting and perfect reflection," *Phys. Rev. Lett.*, vol. 117, no. 25, Dec. 2016, Art. no. 256103.

[10] A. Díaz-Rubio, V. S. Asadchy, A. Elsakka, and S. A. Tretyakov, "From the generalized reflection law to the realization of perfect anomalous reflectors," *Sci. Adv.*, vol. 3, no. 8, Aug. 2017, Art. no. e1602714. [Online]. Available: https://www.science.org/doi/abs/10.1126/sciadv.1602714

[11] C. Yepes, M. Faenzi, S. Maci, and E. Martini, "Perfect non-specular reflection with polarization control by using a locally passive metasurface sheet on a grounded dielectric slab," *Appl. Phys. Lett.*, vol. 118, no. 23, Jun. 2021, Art. no. 231601.

[12] M. Movahediqomi, G. Ptitcyn, and S. Tretyakov, "Comparison between different designs and realizations of anomalous reflectors for extreme deflections," *IEEE Trans. Antennas Propag.*, vol. 71, no. 10, pp. 8007–8017, Oct. 2023.

[13] C. Yepes, S. Maci, S. A. Tretyakov, and E. Martini, "On the role of spatial dispersion in boundary conditions for perfect non-specular reflection," *EPJ Appl. Metamater.*, vol. 9, p. 17, May 2022, doi: 10.1051/epjam/2022015.

[14] H.-X. Xu, G. Hu, X. Kong, Y. Shao, P. Genevet, and C.-W. Qiu, "Super-reflector enabled by non-interleaved spin-momentum-multiplexed metasurface," *Light: Sci. Appl.*, vol. 12, no. 1, p. 78, Mar. 2023.

[15] H.-X. Xu et al., "Interference-assisted kaleidoscopic meta-plexer for arbitrary spin-wavefront manipulation," *Light: Sci. Appl.*, vol. 8, no. 1, p. 3, Jan. 2019.

[16] Y. Meng et al., "Electromagnetic signal modulation by chromatic dispersion in phase gradient metasurface," *IEEE Access*, vol. 10, pp. 90752–90760, 2022.

[17] H.-X. Xu et al., "Tunable microwave metasurfaces for high-performance operations: Dispersion compensation and dynamical switch," *Sci. Rep.*, vol. 6, no. 1, p. 38255, Nov. 2016.

[18] S. Taravati and G. V. Eleftheriades, "Programmable nonreciprocal meta-prism," *Sci. Rep.*, vol. 11, no. 1, p. 7377, 2021.

[19] D. Dardari and D. Massari, "Using MetaPrisms for performance improvement in wireless communications," *IEEE Trans. Wireless Commun.*, vol. 20, no. 5, pp. 3295–3307, May 2021.

[20] A. Oliner and A. Hessel, "Guided waves on sinusoidally-modulated reactance surfaces," *IRE Trans. Antennas Propag.*, vol. 7, no. 5, pp. 201–208, Dec. 1959.

[21] S. N. Tcvetkova, D.-H. Kwon, A. Díaz-Rubio, and S. A. Tretyakov, "Near-perfect conversion of a propagating plane wave into a surface wave using metasurfaces," *Phys. Rev. B, Condens. Matter*, vol. 97, no. 11, Mar. 2018, Art. no. 115447.

[22] S. N. Tcvetkova, S. Maci, and S. A. Tretyakov, "Exact solution for conversion of surface waves to space waves by periodical impenetrable metasurfaces," *IEEE Trans. Antennas Propag.*, vol. 67, no. 5, pp. 3200–3207, May 2019.

[23] S. N. Tcvetkova, E. Martini, S. A. Tretyakov, and S. Maci, "Perfect conversion of a TM surface wave into a TM leaky wave by an isotropic periodic metasurface printed on a grounded dielectric slab," *IEEE Trans. Antennas Propag.*, vol. 68, no. 8, pp. 6145–6153, Aug. 2020.

[24] D.-H. Kwon, "Modulated reactance surfaces for leaky-wave radiation based on complete aperture field synthesis," *IEEE Trans. Antennas Propag.*, vol. 68, no. 7, pp. 5463–5477, Jul. 2020.

[25] H. Lee and D.-H. Kwon, "Printed metasurface leaky-wave antennas based on penetrable aperture field synthesis," *IEEE Trans. Antennas Propag.*, vol. 71, no. 6, pp. 4724–4736, Jun. 2023.

[26] G. Minatti, F. Caminita, M. Casaletti, and S. Maci, "Spiral leaky-wave antennas based on modulated surface impedance," *IEEE Trans. Antennas Propag.*, vol. 59, no. 12, pp. 4436–4444, Dec. 2011.

[27] E. Martini, F. Caminita, and S. Maci, "Double-scale homogenized impedance models for periodically modulated metasurfaces," *EPJ Appl. Metamater.*, vol. 7, p. 12, Jan. 2020, doi: 10.1051/epjam/2020010.

[28] M. Casaletti, "Guided waves on scalar and tensorial reactance surfaces modulated by periodic functions: A circuital approach," *IEEE Access*, vol. 7, pp. 68823–68836, 2019.

[29] G. Minatti, F. Caminita, E. Martini, and S. Maci, "Flat optics for leaky-waves on modulated metasurfaces: Adiabatic Floquet-wave analysis," *IEEE Trans. Antennas Propag.*, vol. 64, no. 9, pp. 3896–3906, Sep. 2016.

[30] T. Arshed, S. Maci, and E. Martini, "Direct synthesis of metasurfaces for efficient space- to surface-wave conversion and beamforming," *IEEE Trans. Antennas Propag.*, vol. 72, no. 10, pp. 7793–7806, Oct. 2024.

[31] B. H. Fong, J. S. Colburn, J. J. Ottusch, J. L. Visher, and D. F. Sievenpiper, "Scalar and tensor holographic artificial impedance surfaces," *IEEE Trans. Antennas Propag.*, vol. 58, no. 10, pp. 3212–3221, Oct. 2010.

[32] A. M. Patel and A. Grbic, "A printed leaky-wave antenna based on a sinusoidally-modulated reactance surface," *IEEE Trans. Antennas Propag.*, vol. 59, no. 6, pp. 2087–2096, Jun. 2011.

[33] G. Minatti et al., "Modulated metasurface antennas for space: Synthesis, analysis and realizations," *IEEE Trans. Antennas Propag.*, vol. 63, no. 4, pp. 1288–1300, Apr. 2015.

[34] D. González-Ovejero, G. Minatti, G. Chattopadhyay, and S. Maci, "Multibeam by metasurface antennas," *IEEE Trans. Antennas Propag.*, vol. 65, no. 6, pp. 2923–2930, Jun. 2017.

[35] M. Faenzi et al., "Metasurface antennas: New models, applications and realizations," *Sci. Rep.*, vol. 9, no. 1, p. 10178, Jul. 2019.

[36] A. Araghi, M. Khalily, P. Xiao, and R. Tafazolli, "Holographic-based leaky-wave structures: Transformation of guided waves to leaky waves," *IEEE Microw. Mag.*, vol. 22, no. 6, pp. 49–63, Jun. 2021.

[37] A. Mehdipour, J. W. Wong, and G. V. Eleftheriades, "Beam-squinting reduction of leaky-wave antennas using Huygens metasurfaces," *IEEE Trans. Antennas Propag.*, vol. 63, no. 3, pp. 978–992, Mar. 2015.

[38] H. Du, Z. Li, M. Chen, and J. Wang, "A broadband fixed-beam leaky-wave antenna," *IEEE Trans. Antennas Propag.*, vol. 71, no. 6, pp. 5434–5439, Jun. 2023.

[39] J. Chen et al., "Wideband leaky-wave antennas loaded with gradient metasurface for fixed-beam radiations with customized tilting angles," *IEEE Trans. Antennas Propag.*, vol. 68, no. 1, pp. 161–170, Jan. 2020.

[40] G. Zhang, Q. Zhang, Y. Chen, and R. D. Murch, "High-scanning-rate and wide-angle leaky-wave antennas based on glide-symmetry Goubau line," *IEEE Trans. Antennas Propag.*, vol. 68, no. 4, pp. 2531–2540, Apr. 2020.

[41] L. Jidi, X. Cao, J. Gao, T. Li, H. Yang, and S. Li, "Ultrawide-angle and high-scanning-rate leaky wave antenna based on spoof surface plasmon polaritons," *IEEE Trans. Antennas Propag.*, vol. 70, no. 3, pp. 2312–2317, Mar. 2022.

[42] Z. Wu, J. Wang, L. Zhao, and Z. Shen, "Full-space and high-scanning rate leaky-wave antenna based on spoof surface plasmon polaritons," *IEEE Antennas Wireless Propag. Lett.*, vol. 23, no. 2, pp. 693–697, Feb. 2024.

[43] K. Achouri and C. Caloz, "Space-wave routing via surface waves using a metasurface system," *Sci. Rep.*, vol. 8, no. 1, p. 7549, May 2018.
[44] D.-H. Kwon and S. A. Tretyakov, "Arbitrary beam control using passive lossless metasurfaces enabled by orthogonally polarized custom surface waves," *Phys. Rev. B, Condens. Matter*, vol. 97, no. 3, Jan. 2018, Art. no. 035439.
[45] J. Budhu, "Near-perfect space-wave to surface-wave coupler enabled conformal space wave transporting metasurfaces," *IEEE Trans. Antennas Propag.*, vol. 72, no. 3, pp. 2540–2554, Mar. 2024.
[46] K.-K. Wong, K.-F. Tong, Z. Chu, and Y. Zhang, "A vision to smart radio environment: Surface wave communication superhighways," *IEEE Wireless Commun.*, vol. 28, no. 1, pp. 112–119, Feb. 2021.
[47] T. Arshed, S. Maci, and E. Martini, "Enhancing reflecting intelligence surface using surface-wave engineering," in *Proc. IEEE INC-USNC-URSI Radio Sci. Meeting (Joint AP-S Symp.)*, Jul. 2024, p. 138.
[48] S. Maci and A. Cucini, "FSS-based EBG surfaces," in *Electromagn. Metamaterials*. Hoboken, NJ, USA: Wiley, 2006, ch. 13, pp. 351–376. [Online]. Available: https://onlinelibrary.wiley.com/doi/abs/10.1002/0471784192.ch13
[49] Z. Chen, H. Deng, Q. Xiong, and C. Liu, "Phase gradient metasurface with broadband anomalous reflection based on cross-shaped units," *Appl. Phys. A, Solids Surf.*, vol. 124, no. 3, p. 281, Mar. 2018, doi: 10.1007/s00339-018-1645-y.
[50] B. Lin, J. Guo, L. Lv, Z. Liu, X. Ji, and J. Wu, "An ultra-wideband reflective phase gradient metasurface using pancharatnam-berry phase," *IEEE Access*, vol. 7, pp. 13317–13325, 2019.
[51] Q. Tong, L. Yu-Rou, and W. Meng-Jun, "Surface wave conversion and conformal transmission based on metasurface," in *Proc. Int. Conf. Microw. Millim. Wave Technol. (ICMMT)*, vol. 1, May 2024, pp. 1–3.
[52] A. Norris and A. Osipov, "Far-field analysis of the Malyuzhinets solution for plane and surface waves diffraction by an impedance wedge," *Wave Motion*, vol. 30, no. 1, pp. 69–89, 1999. [Online]. Available: https://www.sciencedirect.com/science/article/pii/S0165212598000493

**Talha Arshed** (Graduate Student Member, IEEE) was born in Sargodha, Pakistan, in 1990. He received the bachelor's and master's degrees in electrical engineering from the National University of Sciences and Technology (NUST), Islamabad, Pakistan, in 2013 and 2016, respectively, and the Ph.D. degree in electromagnetics from the University of Siena, Siena, Italy, in 2025, with a focus on applied electromagnetics, metasurfaces, and leaky wave structures.

From 2016 to 2019, he was a Lecturer with the University of Engineering and Technology (Taxila), Rawalpindi, Pakistan. Since 2025, he has been a Post-Doctoral Researcher with the University of Siena, working on advanced metasurface-based technologies for next-generation wireless communication systems.

**Stefano Maci** (Fellow, IEEE) received the Laurea degree (cum laude) from the University of Florence, Florence, Italy, in 1987.

He was a co-founder of six spin-off companies. Since 1997, he has been a Professor with the University of Siena, Siena, Italy. In 2004, he joined European School of Antennas (ESoA), as the Founder, a postgraduate school that presently comprises 34 courses on antennas, propagation, electromagnetic theory, and computational electromagnetics, and 150 teachers coming from 15 countries. Since 2004, he has been the Director of ESoA. From 2008 to 2015, he was the Director of the Ph.D. Program in information engineering and mathematics with the University of Siena. His research activity is documented in 200 articles published in international journals (among which 100 on IEEE journals), 14 book chapters, and about 600 papers in proceedings of international conferences. His research interests include high-frequency and beam representation methods, computational electromagnetics, large phased arrays, planar antennas, reflector antennas and feeds, metamaterials, and metasurfaces.

Prof. Maci was a member of the AdCom of the IEEE Antennas and Propagation Society (AP-S), the Board of Directors of European Association on Antennas and Propagation (EurAAP), and the Antennas and Propagation Executive Board of the Institution of Engineering and Technology (IET), U.K. From 2013 to 2015, he was a member of the first National Italian Committee for Qualification to Professor. Since 2000, he has been a member of the Technical Advisory Board of 16 international conferences and the Review Board of six international journals. He was a recipient of the EurAAP Award in 2014, the IEEE Schelkunoff Transaction Prize in 2016, the Chen-To Tai Distinguished Educator Award in 2016, and the URSI Dellinger Gold Medal in 2020. He was the Chair of the Award Committee of IEEE AP-S. He has been the Technical Program Committee (TPC) Chair of the METAMATERIAL 2020 Conference and the General Chairperson of the European Conference on Antennas and Propagation (EuCAP) 2023. From 2004 to 2007, he was a Work Package (WP) Leader of the Antenna Center of Excellence (ACE; FP6-EU), and from 2007 to 2010, he was an International Coordinator of the 24-Institution Consortium of a Marie Curie Action (FP6). He was the Founder and the Director of the consortium FORESEEN, involving 48 European (EU) institutions. He was a Principal Investigator of the Future Emerging Technology Project "Nanoarchitectronics" of the 8th EU Framework Program. He is a Principal Investigator of the EU Program "Metamask." Since 2010, he has been a principal investigator of six cooperative projects and a university coordinator of about other 20 cooperative projects financed by the European Space Agency. He was a Distinguished Lecturer of IEEE AP-S. He was an EuRAAP Distinguished Lecturer of the Ambassador Program. In the last ten years, he has been invited 25 times as a keynote speaker at international conferences. He was the President of the IEEE Antennas and Propagation Society 2023. He was an Associate Editor of IEEE TRANSACTIONS ON ANTENNAS AND PROPAGATION.

**Enrica Martini** (Senior Member, IEEE) was born in Spilimbergo, Italy, in 1973. She received the Laurea degree (cum laude) in telecommunication engineering from the University of Florence, Florence, Italy, in 1998, and the joint Ph.D. degree in informatics and telecommunications and electronics from the University of Florence and the University of Nice-Sophia Antipolis, Nice, France, in 2002.

From 1998 to 1999, she worked at the University of Florence, under a one-year research grant from the Alenia Aerospazio Company, Rome, Italy. In 2002, she was appointed as a Research Associate at the University of Siena, Siena, Italy. She joined the Electromagnetic Systems Section, Ørsted•DTU Department, Technical University of Denmark, until 2007. From 2007 to 2017, she was a Post-Doctoral Fellow with the University of Siena. In 2012, she co-founded the start-up Wave Up Srl, Siena, of which she was the CEO from 2016 to 2018. From 2019 to 2021, she was an Assistant Professor with the University of Siena. She is currently an Associate Professor with the Department of Information Engineering and Mathematics, University of Siena. She coordinated the tasks of various research projects funded by national and international governmental institutions, as well as by industry. Her research interests include metasurfaces and metamaterial characterization, metasurface-based antennas and microwave devices, electromagnetic scattering, antenna measurements, and tropospheric propagation.

Dr. Martini received the Hans Christian Ørsted Postdoctoral Fellowship from the Technical University of Denmark in 2005. She was a co-recipient of the 2016 Schelkunoff Transactions Prize Paper Award, the Best Paper Award in Antenna Design and Applications at the 11th European Conference on Antennas and Propagation in 2017, the Best Poster Award at the Metamaterials Congress in 2019, and the Best Paper Award in Electromagnetics at the 15th European Conference on Antennas and Propagation in 2021.